Novel Soft Smart Shoes for Motion Intent Learning of Lower Limbs using LSTM with a Convolutional Autoencoder

Jiantao Yang, Yuehong Yin, *Member, IEEE*

***Abstract*: Estimating the joint torques of lower limbs in human gait, known as motion intent understanding, is of great significance in the control of lower limb exoskeletons. This study presents novel soft smart shoes designed for motion intent learning at unspecified walking speeds using long short-term memory with a convolutional autoencoder. The smart shoes serve as a wearable sensing system consisting of a soft instrumented sole and two 3D motion sensors that are nonintrusive to the human gait and comfortable for the wearers. A novel data structure is developed as a "sensor image" for the measured ground reaction force and foot motion. A convolutional autoencoder is established to fuse multisensor datasets and extract the hidden features of the sensor images, which represent the spatial and temporal correlations among the data. Then, long short-term memory is exploited to learn the multiscale, highly nonlinear input–output relationships between the acquired features and joint torques. Experiments were conducted on five subjects at three walking speeds (0.8 m/s, 1.2 m/s, and 1.6 m/s). Results showed that 98% of the r^2 values were acceptable in individual testing and 75% of the r^2 values were acceptable in interindividual testing. The proposed method is able to learn the join torques in human gait and has satisfactory generalization properties.**

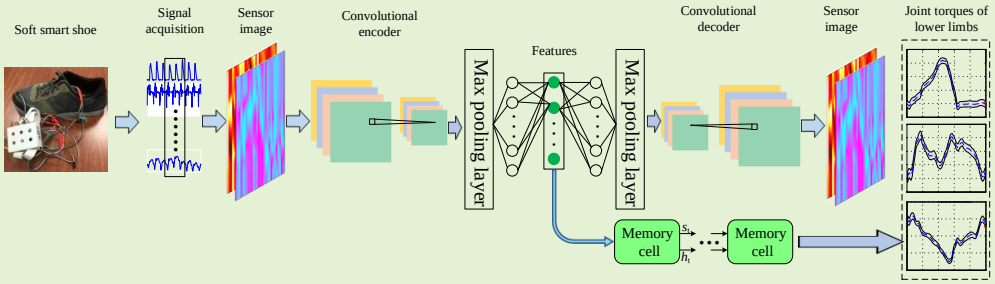

***Index Terms*—convolutional autoencoder, long short-term memory, motion intent learning, soft smart shoes**

I. Introduction

Modern lower limb exoskeleton robots are required to provide compliant motion coordination, or to be "transparent" to users [1]. However, no breakthrough has been made in the field of active compliance and congruent human–machine interaction. Joint torque estimation, known as motion intent understanding, is a precondition of realizing this target [2-4]. Although effective information exchange has been achieved, there are mismatches and disparities in robots' understanding of human motion intent. A cause may be the complexities caused by the modeling of activities in the nervous system, musculoskeletal dynamics, and the cooperation between different joints in the lower extremities. Hence, many reported learning strategies were based on pattern recognition results for simplification [5-6]. This means that they are unable to handle the evolving dynamics, which is not included in the preset classifications. For designing high-level controllers for lower limb exoskeletons, the continuous joint torque estimating studied here may be the better choice as they are of great significance for achieving optimization of exoskeleton assistance [7-8].

Surface electromyography(sEMG) signals have been widely applied to estimate joint torques in the past few years [9-11]. However, the nonstationarity and nonlinearity of physiological signals remain the main obstacles to achieve accurate intent learning and prediction. This calls for a wearable sensing system for the measurement of information on the human gait, which is reliable, comfortable for wearers, and convenient in daily use. As ground reaction force (GRF) and foot motion are the direct indicators of the human gait [12], wearable smart shoes that can measure the plantar pressure and foot motion would be an optimal solution. Additionally, when performing intent learning using smart shoes, understanding the transformation from measured signals to human motion becomes crucial. Thus, the learning algorithm is expected to explore spatial and temporal structures from the inputs and incorporate changes in system dynamics when humans walk at irregular and unspecified speeds.

Continuously estimating joint torque is a highly challenging task due to the time-varying movement features and diversity of gait patterns. Most of the existing methods were unable to cope with the temporal evolution of the human gait using only measurements from smart shoes. Thus, multisensor information

This paragraph of the first footnote will contain the date on which you submitted your paper for review. It will also contain support information, including sponsor and financial support acknowledgment. For example, "This work was supported in part by the U.S. Department of Commerce under Grant BS123456."

All the authors are with the State Key Laboratory of Mechanical System and Vibration, the Robotics Institute, Shanghai Jiao Tong University, Shanghai 200240, (e-mail: JTYang@sjtu.edu.cn; e-mail: yhyin@sjtu.edu.cn).

fusion is recommended to explore dependencies among multiple sensors and figure out the time-varying movement features [13-14]. The emergence of machine learning methods gives rise to the possibility of performing data fusion. Recently, a Convolutional Auto-encoder (CAE), which is effective for finding high-level representations of data, has been used to address the multisensor data fusion problem [15]. Moreover, Long Short-Term Memory (LSTM) exhibits remarkable superiorities in time series signals [16]. These abilities of machine learning methods may be advantageous for the joint torque learning applications.

The rest of this paper is organized as follows: In Section II, a review of previous related works is presented. The novel wearable smart shoes are presented in Section III. The proposed strategy for motion intent learning is presented in Section IV. The experiments and results are reported in Sections V and VI respectively. The discussion and conclusions are presented in Sections VII and VIII respectively.

II. Related work

Extensive research has been conducted on developing wearable smart shoes that can measure plantar pressure and foot motion. These shoes were realized by instrumented insoles or soles combined with inertial measurement units (IMUs). As insole sensors are flexible, lightweight, and nonintrusive to the human gait [17], they were widely used for the measurement of foot pressure [18-19]. He et al. employed a pressure-sensitive electric conductive rubber insole to estimate the knee adduction moment [20]. The design and fabrication of an insole-based gait analysis system were presented in [21]. Evaluation of six control subjects and four hemiplegic stroke subjects was conducted to verify its effectiveness. However, the measurement accuracy of the sole is not satisfactory, which may limit the performance in intent learning [20].

To overcome this limitation, some researchers have focused on soles mounted with force sensors. A smart shoe including an optical three-axis force sensor was developed for joint torque estimation in [22]. Li et al. proposed a novel wearable shoe with commercial force sensors located at the heel, arch, and forefoot, aiming to control exoskeletons in the near future [23]. Unfortunately, these instrumented soles are stiff, which may be intrusive to the human gait and cause discomfort for wearers. Thus, there is an urgent need to develop a soft sole for GRF measurements. Nowadays, soft sensors based on barometers have been presented by many researchers because of the sensitiveness and reliability [24-25]. Soft sensors embedded in a bendable sole module seem to be the better choice [26].

Wearable sensing systems for motion intent learning have been widely studied using machine learning methods including neural networks (NN) [27], the Gaussian process (GP), [4] support vector machines (SVM) [28], etc. For example, autoencoders (AE) was employed to recognize human activities based on wearable sensors [5]. Peng et al. presented a wearable sensor shoe for human falling recognition using the SVM model [28]. These methods are mostly based on pattern recognition results. The learning algorithm needs to explore not only the spatial correlations but also the temporal correlations among datasets for continuously estimating joint torques. Some researchers converted sEMG signals to sEMG images, spatially composed from the high-density sEMG offered by electrode arrays [29]. The dependencies among datasets would be taken into account spatially when processing the sEMG images. Hence, CNN could be used for multisensor information fusion and the extraction of features that were embedded deeply in images. In this study, a novel data structure as a "sensor image" for the measured signals is developed to represent both spatial correlations across datasets and temporal correlations within each dataset [30]. A Convolutional Autoencoder (CAE) is employed to fuse the multisensor datasets and extract the features of "sensor images" [31]. Moreover, LSTM is used for learning both long-term and short-term input–output relationships with improved accuracy and efficiency. Therefore, excellent performance may be achieved by integrating these approaches and making use of their benefits.

The aim of this paper is to present a novel soft wearable shoe for motion intent learning. The smart shoe consists of a soft sole with pneumatic sensors and two 3D motion sensors to acquire information concerning GRF and foot motion. The novel shoes are nonintrusive to the human gait and comfortable to wearers. In addition, a new initiative via Long Short-Term Memory with a Convolutional Autoencoder (LSTM with CAE) to estimate joint torques is developed. Firstly, multisensor data are constructed as a "sensor image" that can represent the spatial and temporal structures among the datasets. Then the Convolutional Autoencoder (CAE) is incorporated to fuse the multisensor datasets and extract features from 2D images. Finally, LSTM is exploited to learn the temporal evolution of human gait in the long term, and model the highly nonlinear input–output relations in the short term. The proposed learning method is devoted to figuring out the deep-layer relationships among the multisource information comprehensively. Thus, the learning of human motion intent can be achieved at unspecified walking speeds. Experimental works are also presented to demonstrate the superior performance and generalizability of the proposed method.

III. Wearable smart shoes

The novel smart shoe shown in Fig. 1 is developed with a soft sole, two 3D motion sensors, and a self-designed data acquisition instrument to replace the conventional gait measurement system used in the laboratory. Fig. 2 demonstrates the structure of the sole. The sole presented in this study was made of silicone rubber with Hardness Shore 35A (Ecoflex 0035, SmoothOn Inc., USA). A fiber-reinforced structure in the elastomeric matrix using fiberglass was adopted for the upward-facing surface of the sole [32]. Thus, the radial expansion of the upward-facing surface was limited to supply uniform pressure. There were three pneumatic chambers at the heel, arch, and forefoot, since the major weight is distributed to the heel and forefoot in case of a normal gait and pressures under the arch help to detect the mid-stance phase [33-34]. Several columns were set up in the chambers based on the plantar anatomy and pressure distribution. A barometer with accuracy ±1.5 mbar and resolution 0.024 mbar (MS5637-02BA03, Measurement Specialties Inc, Switzerland) was enclosed in the chamber to measure the air pressure. When wearers walk on the ground, the pneumatic chamber is compressed, which is associated with the GRF, resulting in pressure changes in the air

chamber. The 3D motion sensor (MPU9250, InvenSense, USA) was developed with a gyroscope, an accelerometer, and a magnetometer. An extended Kalman filter was adopted to fuse the measurements and provide the foot motion. A Kalman filter consists of prediction and update of the state vector, which is widely used in wearable sensors [12,23]. A brief description of this method is as follows.

The orientation is represented by the quaternion $\boldsymbol{q}=\begin{bmatrix} q_0 & q_1 & q_2 & q_3 \end{bmatrix}^T$. The state equation can be written as follows [22]:

$$\hat{\boldsymbol{q}}(k)=\boldsymbol{\Phi}(k)\cdot\boldsymbol{q}(k-1)+\nu(k-1) \tag{1}$$

where $\Phi_{k,k-1}$ is the state transition matrix, described as

$$\boldsymbol{\Phi}(k)=\frac{1}{2}\begin{bmatrix} 2 & -\omega_k^x T & -\omega_k^y T & -\omega_k^z T \\ \omega_k^z T & 2 & \omega_k^y T & -\omega_k^z T \\ \omega_k^y T & -\omega_k^z T & 2 & \omega_k^x T \\ \omega_k^z T & \omega_k^y T & -\omega_k^x T & 2 \end{bmatrix} \tag{2}$$

where T is the sampling period, and ω_k^x, ω_k^y and ω_k^z are the angular velocities measured along the X-axis, Y-axis, and Z-axis by the gyroscope at the kth step. The accelerations $\boldsymbol{z}(k)$ measured by the accelerometer at the kth step are used to update the state vector as follows:

$$\boldsymbol{q}(k)=\hat{\boldsymbol{q}}(k)+\boldsymbol{K}(k)\left(\boldsymbol{z}(k)-\boldsymbol{H}(k)\hat{\boldsymbol{q}}(k)\right) \tag{3}$$

where $\boldsymbol{H}(k)=\frac{\partial \boldsymbol{z}}{\partial \boldsymbol{q}}|_{\hat{\boldsymbol{q}}(k)}$. $\boldsymbol{K}(k)$ can be updated by the following equations:

$$\boldsymbol{K}(k)=\hat{\boldsymbol{P}}(k)\boldsymbol{H}^T(k)\left(\boldsymbol{H}(k)\hat{\boldsymbol{P}}(k)\boldsymbol{H}^T(k)+\boldsymbol{R}\right)^{-1} \tag{4}$$

$$\hat{\boldsymbol{P}}(k)=\boldsymbol{\Phi}(k)\boldsymbol{P}(k-1)\boldsymbol{\Phi}^T(k)+\boldsymbol{Q} \tag{5}$$

where $\boldsymbol{R}$ and $\boldsymbol{Q}$ are the measurement noise and the state covariance matrix, respectively. $\boldsymbol{P}$ is updated as follows:

$$\boldsymbol{P}(k)=\left(\boldsymbol{I}-\boldsymbol{K}(k)\boldsymbol{H}(k)\right)\hat{\boldsymbol{P}}(k) \tag{6}$$

A microprocessor (STM32f103, STMicroelectronics Inc., Switzerland) with industrial ARM Cortex-M3 core and a WIFI module (CC3200R1M2, Texas Instruments Inc, USA) were integrated into a printed circuit board for data acquisition. The air pressures, orientations (accuracy of ±0.01°) of the heel and forefoot, and angular velocities (accuracy of ±0.05°) of the heel and forefoot were acquired with a sampling rate of 100 Hz and then transported to a personal computer by the WIFI module on the data acquisition instrument.

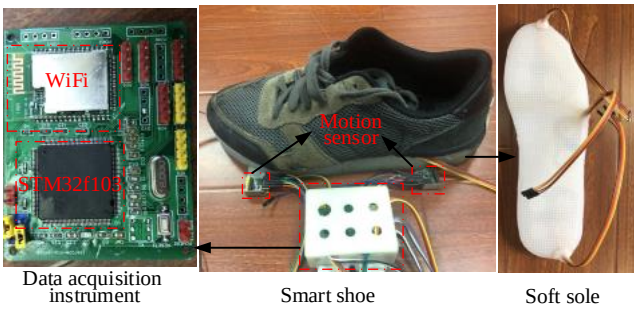

Fig 1. The wearable smart shoe.

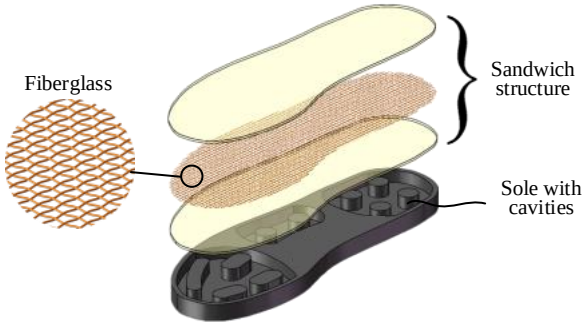

Fig. 2. Structure of the sole.

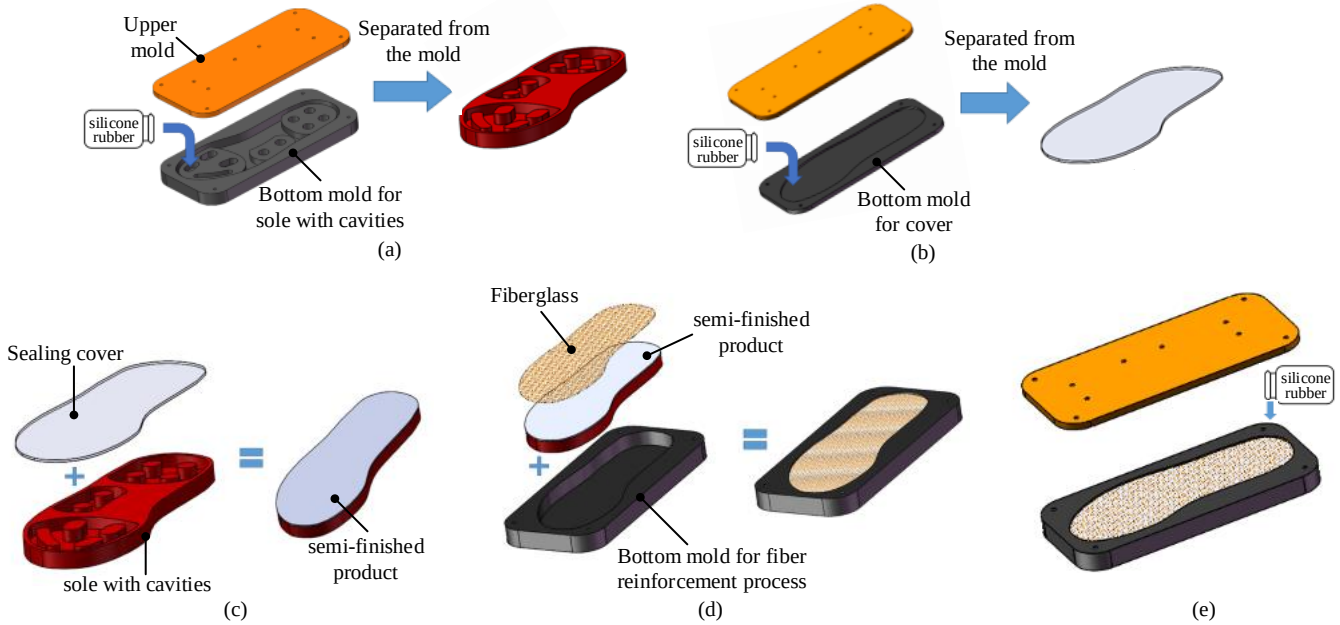

Fig. 3. Multistep molding approach for fabricating the sole.

The fiber-reinforced sole was fabricated by the multistep molding approach shown in Fig. 3, which was always used for fabricating soft actuators and sensors [35]. The molds (i.e., the bottom and upper molds) with cavity were designed by CAD software and could be easily fabricated by 3D printing; there were air vents placed on the upper mold (Fig. 3a) to reduce the bubbles trapped in the cured silicone. The silicone rubber included two parts, e.g., A and B. Part A and Part B should be mixed at a ratio of 1:1. Then, the mixture was poured into the bottom mold, and placed in a vacuum chamber for 10 min to remove the bubbles. Next, the bottom and upper molds were fastened together by screws. Finally, the entire assembly was put into the oven at 50 °C for 30 min until the rubber was cured.

After molding the sole with cavities (Fig. 3a) and a cover (Fig. 3b) using the above fabrication process, three barometers were placed in every cavity. The sole with cavities and cover could be glued together easily by the same silicone rubber to form the semifinished product (Fig. 3c). In the third stage, the semifinished product was put into another mold, and fiberglass was attached on the upward-facing surface (Fig. 3d). Finally, a fiber-reinforced structure for supplying uniform pressure was realized by pouring the silicone rubber into a mold to encapsulate the fiberglass in a 2.0-mm-thick silicone layer (Fig. 3e). The air sensors and fiberglass were fully encapsulated because the entire sole was made of identical material. The final structure of the sole shown in Fig. 2 includes a fiber-reinforced part in a “sandwich configuration” . The soft sole has numerous advantages, e.g., nonintrusive to the human gait, comfortable to the wearers, and low cost.

IV. METHODOLOGY

In this section, the proposed strategy for motion intent learning is presented in detail. The aim of the model is to predict the output of a dynamic system given n measured previous system states $\boldsymbol{x}$, which can be expressed as $y_k = f(\boldsymbol{x})$. The LSTM with CAE is adopted here to learn the nonlinear function f. As shown in Fig. 4, the methodology consists of three parts, i.e., construction of sensor images from measured data, CAE for data fusion and feature extraction, and prediction by LSTM. The inputs of the model are the constructed sensor images and the outputs are the joint torques at the ankle, knee, and hip. The average time cost for estimating torques at a certain moment is about 2 ms when the predictor is developed using TensorFlow 2.0 and runs on a laptop (ThinkServer TS250 from Lenovo Ltd., China).

The novel smart shoes were used for the measurement of the system states during human walking. The air pressures of the sole did not need to be calibrated to establish a mapping between air pressures and GRFs, since the proposed LSTM with CAE was a data-driven method. The raw signals could provide more information compared to the final resultant GRFs. A set of measured data as $\boldsymbol{x}_l = \left[\boldsymbol{x}_1^T \ \cdots \ \boldsymbol{x}_{15}^T\right]^T \in \mathbb{R}^{15\times n}$ from left shoe can be acquired including three air pressures, three orientations, and three angular velocities of the heel, and three orientations and angular velocities of the forefoot, where $\boldsymbol{x}_i = \left[x_{i1} \ \cdots \ x_{in}\right]^T \in \mathbb{R}^{n\times 1}$ (i=1,2, ⋯ ,15) is the acquired signals of a sensor. $\boldsymbol{x}_1$, $\boldsymbol{x}_2$ and $\boldsymbol{x}_3$ represent the air pressures in the three pneumatic chambers at the heel, arch, and forefoot, respectively. $\boldsymbol{x}_4$, $\boldsymbol{x}_5$ and $\boldsymbol{x}_6$ denote the attitude angles of the heel along the X-axis, Y-axis, and Z-axis, respectively. $\boldsymbol{x}_7$, $\boldsymbol{x}_8$ and $\boldsymbol{x}_9$ are the angular velocities of the heel along the X-axis, Y-axis, and Z-axis, respectively. $\boldsymbol{x}_{10}$, $\boldsymbol{x}_{11}$ and $\boldsymbol{x}_{12}$ are the attitude angles of the forefoot along the X-axis, Y-axis, and Z-axis, respectively. $\boldsymbol{x}_{13}$, $\boldsymbol{x}_{14}$ and $\boldsymbol{x}_{15}$ are the angular velocities of the forefoot along the X-axis, Y-axis, and Z-axis, respectively.

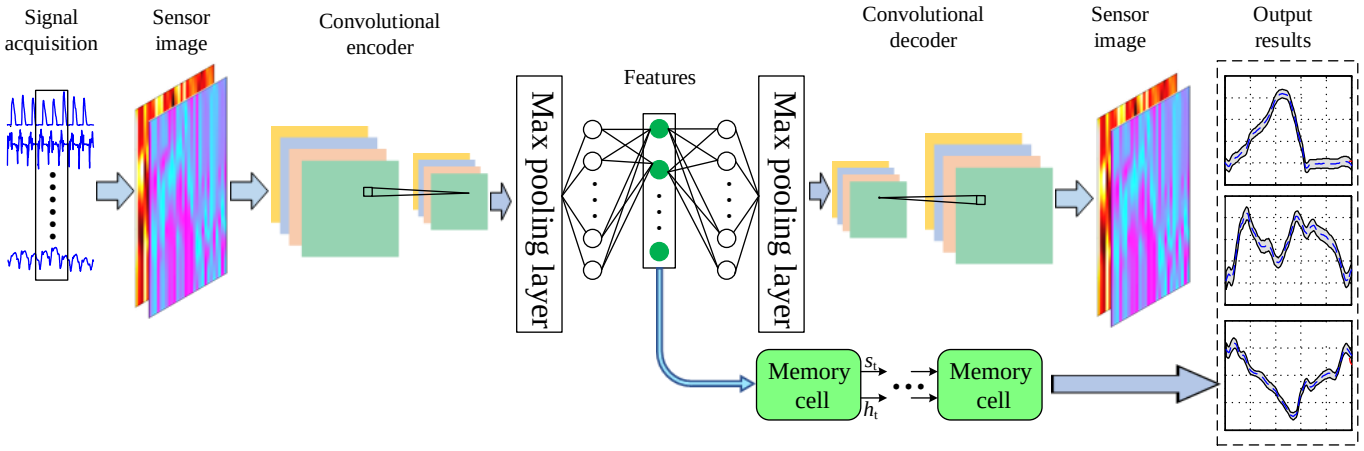

Fig. 4. Architecture of the proposed LSTM with CAE.

Similarly, the data measured from the right shoe are denoted as $\boldsymbol{x}_r = \left[\boldsymbol{x}_{16}^T \ \cdots \ \boldsymbol{x}_{30}^T\right]^T \in \mathbb{R}^{15\times n}$. Thus, the model input can be represented as $\tilde{\boldsymbol{x}} = \left[\boldsymbol{x}_l^T \ \ \boldsymbol{x}_r^T\right]^T$. The raw signals should be standardized by subtracting the mean $\boldsymbol{x}_m$ and dividing them by the standard deviation $\boldsymbol{\sigma}_m$ using Equation (7) as many deep learning methods do [36].

$$\hat{\boldsymbol{x}} = \frac{\tilde{\boldsymbol{x}} - \boldsymbol{x}_m}{\boldsymbol{\sigma}_m} \tag{7}$$

The multisensor data measured by smart shoes definitely

have dependencies. In order to explore the deep-layer structures among the data, a sensor image was constructed using n measured previous system states $\hat{\boldsymbol{x}}$ as shown in Fig. 5. The X-axis of the image represents the timeline. The Y-axis is the multiple sensors. The image defined in this study can represent the temporal and spatial correlations among the measured data. After numerous attempts, it was found that the prediction accuracy and computation cost were most balanced at n = 28.

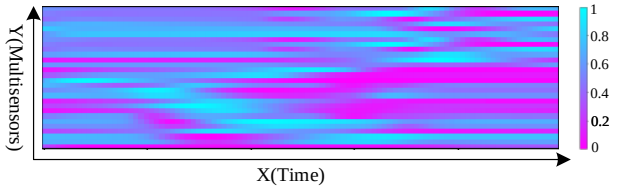

Fig. 5. The sensor image.

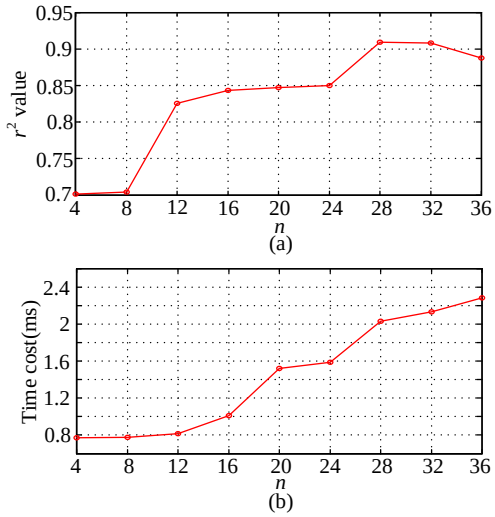

Fig. 6. (**a**) r^2 values with different n; (**b**) average time cost for 1000 prediction points with different n.

Fig. 6 illustrates the r^2 values and average time cost for 1000 prediction points with different n in a typical experiment. It can be inferred that the time cost increases with increased n. When the window width is short, the performance is unacceptable. However, when the window width is larger than 28, the performance may not be obviously improved, and the computational complexity increases correspondingly. Thus, considering the performance and time cost, n = 28 is the best choice. The sensor image is generated as a 28*30 matrix. More specifically, the measured data from the previous n sampling periods for each sensor can be regarded as a column vector $\boldsymbol{x}_i$, $i = 1, 2, \cdots, 30$. These vectors are constructed as a matrix denoted as $\tilde{\boldsymbol{x}}$, whose elements can be referred to as pixels of an image. This allows for using CAE to process signals in the same way as processing images.

As illustrated in Fig. 4, a CAE is an unsupervised neural network consisting of two stages, encoding and decoding, whose parameters are learned automatically in terms of the given data. The encoder transforms inputs into abstract features. The decoder is an inverse of the encoder, reconstructing the inputs from the acquired features. Thus, high-dimensional data are squeezed into low-dimensional features. The weights are adjusted using backpropagation to minimize reconstruction error:

$$E = \sum_{i=1}^{n} \left(\hat{\boldsymbol{x}}_i - \boldsymbol{y}_i \right)^2 \tag{8}$$

where $\hat{\boldsymbol{x}}_i$ and $\boldsymbol{y}_i$ are the input and the reconstructed input, respectively. CNN is one of the most popular methods to process images in the deep learning field and has the characteristic of scale invariance. It is adopted here to extract the local features, which represent the location correlations among the measured data [37]. Square 3 × 3 trainable filters were used for the convolution layers, since there were no differences between the horizontal and vertical dimensions [38]. Rectified linear unit (ReLU) was always prioritized as the activation function, as it facilitated the training process without losing accuracy. Subsequently, a max-pooling process was included to find the maximum pixel among every four neighboring pixels. The pooling layers enable exploring the secondary features, which can decrease the spatial resolution to extract multiscale features from human motion. Then, a dense layer was added to deal with the nonlinearity of the learned function. The detailed architecture of the CAE is given in Table 1.

TABLE I
THE ARCHITECTURE OF THE CAE.

Layer	Conv1	Conv2		
Kernel size	3 × 3	3 × 3	Max pooling	Dense
Number of kernels	16	8		
stride	1	1		
pad	1	1		

To enhance the robustness of CAE, stochastic mapping $\boldsymbol{\chi} \sim D(\boldsymbol{\chi} \mid \hat{\boldsymbol{x}})$ was applied to the input matrix $\hat{\boldsymbol{x}}$ to get a destroyed vision $\boldsymbol{\chi}$ which served as denoising coding. Then the neural network was trained to reconstruct the input form the partially destroyed one. More specifically, for each input $\hat{\boldsymbol{x}}$, a desired proportion of components was chosen randomly to be 0, while the others were left unchanged. Then, the corrupted input $\boldsymbol{\chi}$ was coded to a hidden representation $\boldsymbol{h} = f_\theta(\boldsymbol{\chi})$, from which $\boldsymbol{z} = g_\theta(\boldsymbol{h})$ could be reconstructed. Therefore, the cost function, minimized by the stochastic gradient descent, was set to

$$\arg\min E\left[L\left(\boldsymbol{x}, g_\theta\left(f_\theta(\boldsymbol{\chi}) \right) \right) \right] \tag{9}$$

where $L\left(\boldsymbol{x}, g_\theta\left(f_\theta(\boldsymbol{\chi}) \right) \right)$ is the reconstruction error.

Generally speaking, overfitting often occurs when the training dataset is insufficient, which may lead to poor prediction results for the test data. To combat the overfitting problem, a dropout technique was adopted to train the CAE network by randomly masking the output of some hidden neurons, which would avoid the extraction of the same features repeatedly [31]. Specifically, these masked neurons would not be involved in the forward propagation training process.

LSTM belongs to the class of recurrent neural networks (RNN). It was designed to explore the long-term and short-term dependencies of time series problems and attempted to address the deficiencies, i.e., vanishing and exploding gradients, encountered by RNN. These characteristics are especially desirable for joint torque estimation in the robotic domain. A LSTM network consists of an input layer, one or more recurrent

hidden layer(s), and an output layer. The basic unit of memory cell of the hidden layer represents the main characteristic of the LSTM. As shown in Fig. 7, a memory cell has three gates: a forget gate, an input gate, and an output gate.

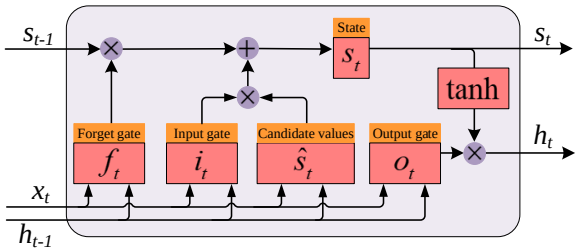

Fig. 7. LSTM network.

Here, the following notation is used:

- $\boldsymbol{x}_t$ is the input at timestep *t*.
- $\boldsymbol{b}_f$, $\boldsymbol{b}_i$, $\boldsymbol{b}_{\hat{s}}$ and $\boldsymbol{b}_o$ denote the bias vectors.
- $\boldsymbol{h}_t$ is the output of the LSTM model.
- $\boldsymbol{W}_{f,x}$, $\boldsymbol{W}_{f,h}$, $\boldsymbol{W}_{i,x}$, $\boldsymbol{W}_{i,h}$, $\boldsymbol{W}_{o,x}$,and $\boldsymbol{W}_{o,h}$ are weight matrices.
- ∘ denotes the Hadamard product.

The forget gate $\boldsymbol{f}_t$ specifies which information should be removed from the previous cell states $\boldsymbol{s}_{t-1}$. The current input $\boldsymbol{x}_t$ and the output $\boldsymbol{h}_{t-1}$ of the previous timestep *t*-1 are used as the inputs of the forget gate, which scales all activation values into the range between 0 and 1 using a sigmoid function:

$$\boldsymbol{f}_t = \boldsymbol{\sigma}\left(\boldsymbol{W}_{f,x}\boldsymbol{x}_t + \boldsymbol{W}_{f,h}\boldsymbol{h}_{t-1} + \boldsymbol{b}_f\right) \tag{10}$$

where $\boldsymbol{\sigma}$ is the logistics sigmoid function.

The input gate $\boldsymbol{i}_t$ determines which information should be incorporated into the current cell state $\boldsymbol{s}_t$. The output of the input gate is calculated using the following equation:

$$\boldsymbol{i}_t = \boldsymbol{\sigma}\left(\boldsymbol{W}_{i,x}\boldsymbol{x}_t + \boldsymbol{W}_{i,h}\boldsymbol{h}_{t-1} + \boldsymbol{b}_i\right) \tag{11}$$

In addition, candidate value $\hat{\boldsymbol{s}}_{t-1}$ may potentially be added to the cell state as follows:

$$\hat{\boldsymbol{s}}_t = \tanh\left(\boldsymbol{W}_{\hat{s},x}x_t + \boldsymbol{W}_{\hat{s},h}\boldsymbol{h}_{t-1} + \boldsymbol{b}_{\hat{s}}\right) \tag{12}$$

Based on the results of Equations (10) and (11), the current cell state is denoted as follows:

$$\boldsymbol{s}_t = \boldsymbol{f}_t \circ \boldsymbol{s}_{t-1} + \boldsymbol{i}_t \circ \hat{\boldsymbol{s}}_t \tag{13}$$

Finally, the output gate indicates what information relating the cell state should be used as the output:

$$\boldsymbol{o}_t = \boldsymbol{\sigma}\left(\boldsymbol{W}_{o,x}\boldsymbol{x}_t + \boldsymbol{W}_{o,h}\boldsymbol{h}_{t-1} + \boldsymbol{b}_o\right) \tag{14}$$

$$\boldsymbol{h}_t = \boldsymbol{o}_t \circ \tanh\left(\boldsymbol{s}_t\right) \tag{15}$$

V. Experimental Study

A. Subjects

The shoe size should be appropriate for wearers to ensure comfort. Thus, the shoe size of the subjects should not vary greatly. As a group of four to eight subjects was used in many reported smart shoes to validate the method [12,20,23,26], five subjects, denoted as A–E, without musculoskeletal or neurological dysfunctions gave written informed consent prior to participation in the experiments. The general information about the subjects is given in Table 2.

TABLE II Subjects' Information Used in This Study (Mean ± Standard Deviation)

Number of subjects	Age (years)	Height (cm)	Mass (kg)	Shoe Size (Chinese)
5	26.3 ± 3.4	176.4 ± 5.3	63.3 ± 3.1	41.6 ± 1.0

B. Experimental protocol

In order to verify the performance and effectiveness of the developed shoes for intent learning, a reference system composed of an optical motion capture system (from Vicon Inc.) and a treadmill that had independent belts and dual force plates to measure the ground reaction force/moment for each foot was used as shown in Fig. 8. Sixteen markers were fixed on the following anatomical landmarks of the subject: right anterior superior iliac, right posterior superior iliac, right thigh, right knee, right tibia, right ankle, right heel, right toe, left anterior superior iliac, left posterior superior iliac, left thigh, left knee, left tibia, left ankle, left heel, and left toe. Twelve high-speed motion capture cameras were used to capture the markers on the lower limbs. The signals were acquired with a sampling rate of 100 Hz. After a practice, all the subjects were required to wear smart shoes with size 42 (European size) and walk on the treadmill at three walking speeds (0.8 m/s, 1.2 m/s, and 1.6 m/s). Four trials denoted as Trial 1 to Trial 4 at each speed were conducted. A set of measured data as $\tilde{\boldsymbol{x}} \in \mathbb{R}^{30\times n}$ from each shoe can be acquired including three air pressures, three orientations, and three angular velocities of the heel, and three orientations and angular velocities of the forefoot. The datasets of Trials 1–4 for each speed were composed of 5000 points. Data of Trial 1 (relating to the three walking speeds) were used for training the CAE model. Then, features extracted from data of Trial 2 (relating to the three walking speeds) using the trained CAE model were treated as the inputs to the LSTM for training. The verifying experiments were performed in two modes, including individual testing and interindividual testing. For individual testing, data from Trial 3 were used for validating, and the model should be trained with the data of the same subject. For interindividual testing, data of Trial 4 were used for validating, and the model should be trained with the data of another subject.

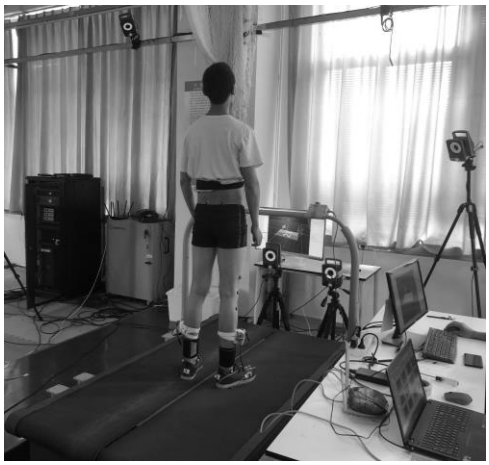

Fig. 8. The subject and experimental setup.

C. Data processing

Force plate data (three-dimensional ground reaction force

and three-dimensional ground reaction moment for each foot) and marker data (positions in three-dimensional space) were recorded and processed by Nexus 2.5 software (Vicon, Inc.), in which joint torques could be found. The joint torques were normalized by body weight [39]. The raw signals $\tilde{x}$ from smart shoes were standardized by subtracting their mean x_m and divided by the standard deviation σ_m using Equation (7). The proposed LSTM with CAE model was developed using TensorFlow 2.0 and ran on a laptop (ThinkServer TS250 from Lenovo Ltd.). RMSE (Root mean square error) between the estimated values and expected values was calculated to evaluate the learning quality. The RMSE contains information about the distribution of the estimated values around the expected values. In addition, the correlation coefficient (r^2 value) was also computed to provide a more comprehensive understanding of the results. These measures have been mentioned in different studies [40]. The criterion used in [41] was that the r^2 value higher than 0.8 was regarded as the acceptable estimation. The r^2 values and RMSEs give a comprehensive understanding of the estimation results.

VI. Results

A. Analysis of denoising coding and dropout

Denoising coding merging in CAE can ensure robust feature extraction and improve the performance of the model. On the one hand, corruption noise may avoid the identity transformation. It is motivated by the idea of "salt noise" in image processing. Therefore, the robustness of feature extraction may be guaranteed. On the other hand, the corruptions of inputs can be seen as a way of artificially expanding data samples. Thus, the performance of the model may be improved.

The level of corruption noise is a hyperparameter in CAE. Thus, the effect of corruption noise strength on the final results should be studied. After numerous attempts, it was found that when the denoising rate was 0.3, the best performance was achieved. Fig. 9 illustrates the performance with different corruption in a typical experiment. The noise levels were changed from 0 to 0.5 with a step size of 0.1. Higher r^2 value and lower RMSE could be obtained when using a proper denoising rate, as shown in Fig. 8. Otherwise, it leads to a decrease in the estimating performance. More specifically, gentle corruption noise would deteriorate the robustness of the model, resulting in unsatisfactory performance. Meanwhile, too much corruption noise might degrade the quality of the inputs, leading to a decrease in performance. It can be concluded that CAE trained with appropriate noisy data can extract more robust features, which is of great significance in practical use.

The effect of dropout on the final results was also studied. Fig. 10 shows a typical experiment when the dropout rate was 0 to 0.5 with a step size of 0.1. It was found that when the dropout rate was 0.2, the best performance was achieved. Dropout higher than 0.2 might lose some important neurons for feature representation, resulting in a decrease in accuracy. In summary, we can draw the conclusion that CAE with denoising coding and using the dropout technique in the training process can extract more robust features and overcome the overfitting problem. Thus, satisfactory performance can be achieved, as expected.

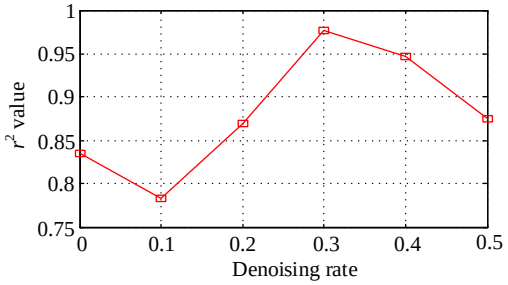

(a) Effect of denoising coding on r^2.

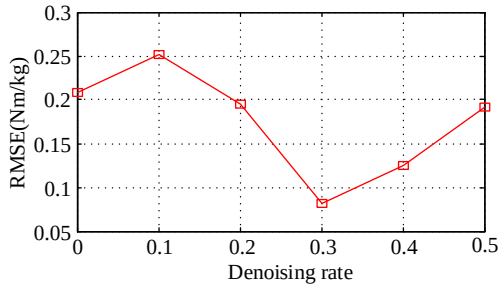

(b) Effect of denoising coding on RMSE.

Fig. 9. Studies on denoising coding.

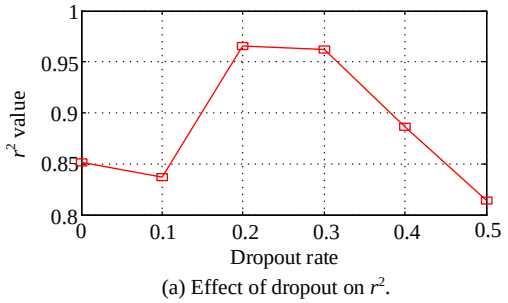

(a) Effect of dropout on r^2.

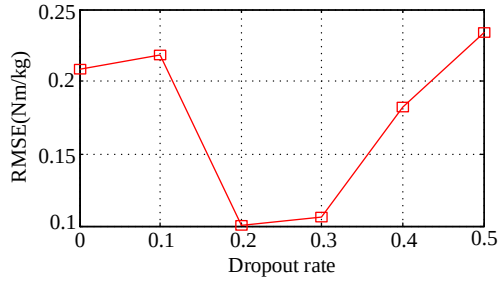

(b) Effect of dropout on RMSE.

Fig. 10. Studies on dropout.

B. Individual testing

Fig. 11 demonstrates a typical set of experimental results in individual testing, presented as percentages of the gait cycle from heel contact, where the estimated results are denoted in blue dotted lines and the expected joint torques are denoted in red solid lines. As shown in Fig. 11, the results are quite acceptable, with all the r^2 values higher than 0.8. This is representative and typical for most of the subjects.

r^2 values relating to the three walking speeds (0.8 m/s, 1.2 m/s, and 1.6 m/s) for each subject are listed in Table 3. Only one (underlined in Table 3) value out of 45 is unacceptable. About 53% of the r^2 values are greater than 0.9, which shows the superiority of the algorithm. The results indicate that the proposed method is able to learn joint torques of lower limbs when subjects walk at unspecified speeds.

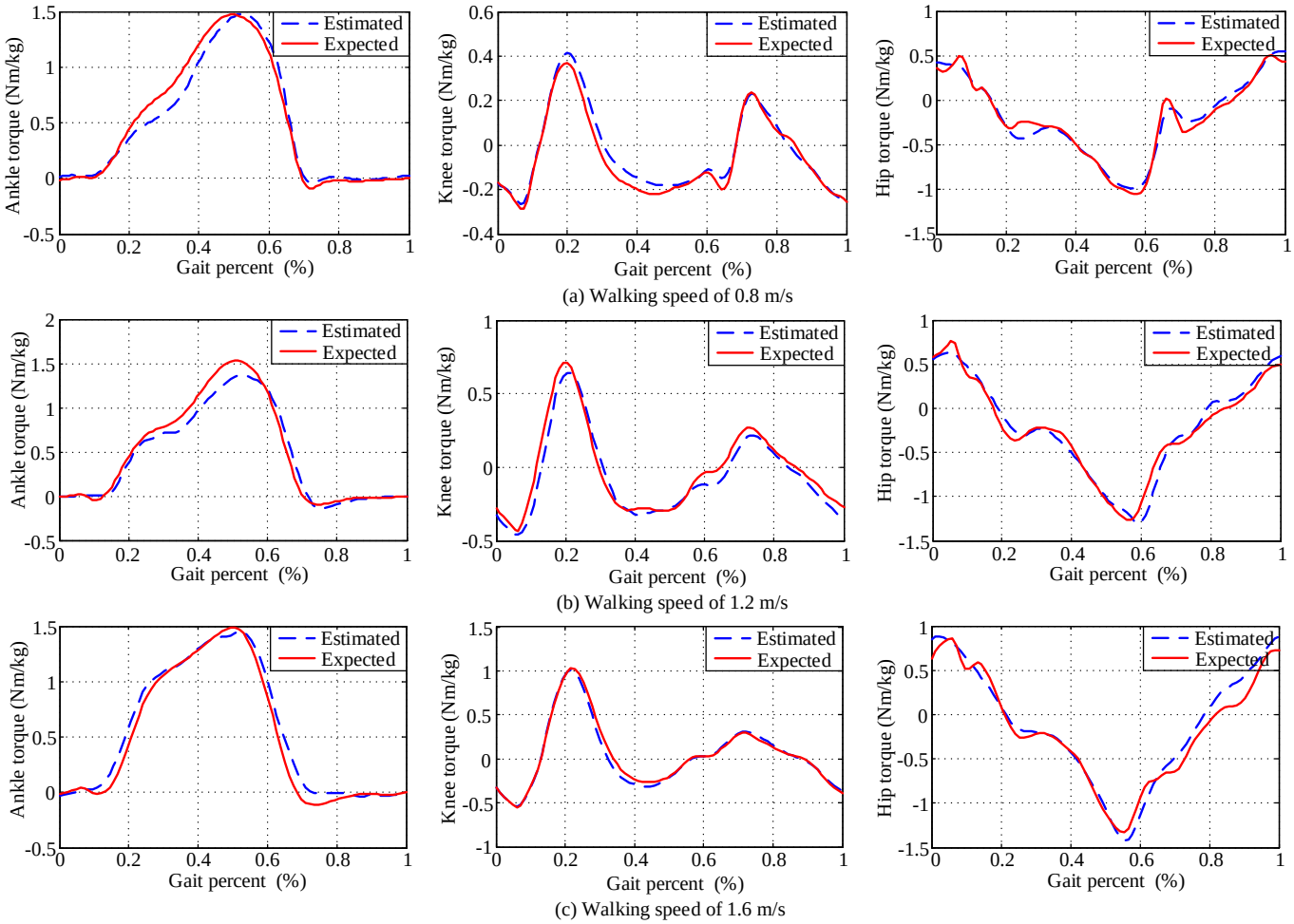

Fig. 11. Estimation results of joint torques at walking speed of 0.8 m/s, 1.2 m/s, and 1.6 m/s.

TABLE III

R^2 VALUES RELATING TO THE THREE WALKING SPEEDS.

Subject	0.8 m/s			1.2 m/s			1.6 m/s		
	Ankle	Knee	Hip	Ankle	Knee	Hip	Ankle	Knee	Hip
A	0.8501	0.8898	0.8937	0.8853	0.8825	0.8990	0.9278	0.9716	0.9033
B	0.9257	0.8918	0.9238	0.9076	0.8498	0.9433	0.9461	0.8599	0.9810
C	0.8781	0.8501	0.9039	0.9232	0.8767	0.8302	0.9579	0.8506	0.9621
D	0.9238	0.9353	0.8738	0.9541	0.9137	0.9703	0.9723	0.8845	0.9422
E	0.8842	0.9074	0.8983	0.9803	0.8922	0.9644	0.8830	0.7715	0.9138

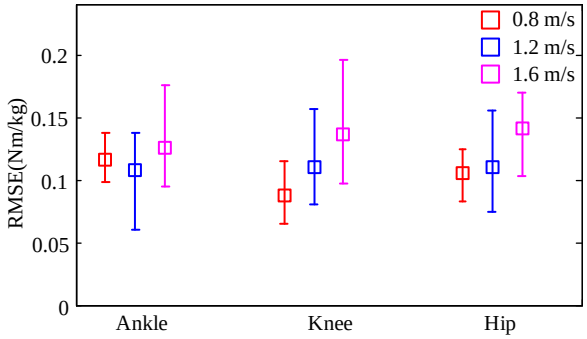

Figure 12. Mean, maximal, and minimal values of RMS errors.

The RMSEs are illustrated in Fig. 12. The squares show the mean RMSEs of the five subjects at each speed. The upper and lower bounds are the maximal and minimal RMSE values, respectively, of the five subjects. The average RMSEs of ankle joint torques, knee joint torques, and hip joint torques at a walking speed of 0.8 m/s were 0.1167 Nm/kg, 0.0877 Nm/kg, and 0.1055 Nm/kg. The maximal RMSEs of the three joints at this walking speed were 0.1381 Nm/kg, 0.1155 Nm/kg, and 0.1248 Nm/kg, implying a good agreement between the estimation and the reference. The RMSEs at walking speed of 1.2 m/s also indicated good agreement between the estimation and the reference, with average values of 0.1085 Nm/kg, 0.1105 Nm/kg, and 0.1101 Nm/kg for the ankle, knee, and hip.

The maximal RMSEs of the three joints at this walking speed were 0.1380 Nm/kg, 0.1565 Nm/kg, and 0.1564 Nm/kg. The RMSEs at a walking speed of 1.6 m/s were also acceptable. The average RMSEs at a walking speed of 1.6 m/s were 0.1265 Nm/kg, 0.1371 Nm/kg, and 0.1417 Nm/kg. The maximal RMSEs of the three joints at this walking speed were 0.1767 Nm/kg, 0.1964 Nm/kg, and 0.1702 Nm/kg. As seen in Fig. 12, the RMSEs of the ankle were lower and fluctuated narrowly compared with the other two joints. The RMSEs of the hip joint were the highest of the three.

C. Interindividual testing

Interindividual testing was conducted to verify the generalization of proposed torque learning method. The results of subject A mean that the measurements of subject A were used for predictions, while measurements from subject B were used for training the model. Others were conducted in the same way. The results of subject E mean that the measurements of subject E were used for predictions, and measurements from subject A were used for training the model. This testing method was also used in [2,23].

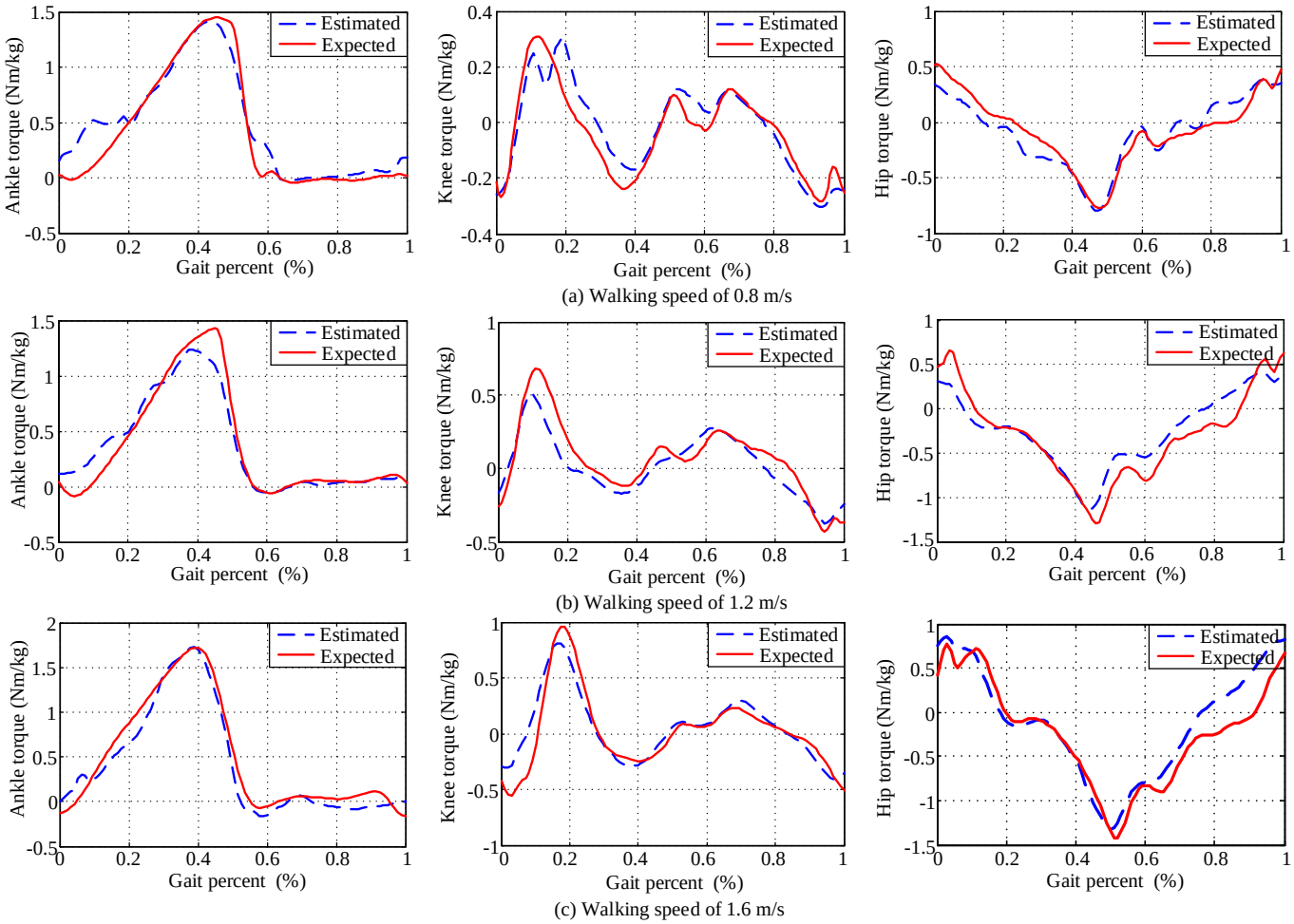

(a) Walking speed of 0.8 m/s

(b) Walking speed of 1.2 m/s

(c) Walking speed of 1.6 m/s

Fig. 13. Estimation results of inter-individual testing.

TABLE V R^2 VALUES OF INTERINDIVIDUAL TESTING.

Subject	0.8 m/s			1.2 m/s			1.6 m/s		
	Ankle	Knee	Hip	Ankle	Knee	Hip	Ankle	Knee	Hip
A	0.7533	0.8176	0.7048	0.7598	0.7627	0.8073	0.7464	0.5108	0.7822
B	0.8262	0.8801	0.8735	0.8923	0.7897	0.8340	0.9247	0.7801	0.8920
C	0.9090	0.8144	0.8826	0.9383	0.8758	0.8922	0.9169	0.8220	0.9145
D	0.8132	0.8213	0.8940	0.8917	0.8617	0.8877	0.9334	0.9313	0.9514
E	0.8935	0.8723	0.7191	0.8544	0.7148	0.8723	0.8408	0.8211	0.9173

Fig. 13 demonstrates a typical set of experimental results of interindividual testing presented as percentages of the gait cycle from heel contact, where the estimated results are denoted in blue dotted lines and the expected joint torques are denoted in red solid lines. The results of interindividual testing are not as good as those of individual testing, which is expected and

agrees with the conclusions in [23].

The r^2 values relating to the three walking speeds (0.8 m/s, 1.2 m/s, and 1.6 m/s) for each subject are listed in Table 4. The r^2 values of subjects B, C, D, and E are almost acceptable. However, the r^2 values of the subject A are not so good.

The RMSEs are illustrated in Fig. 14. The squares show the mean RMSEs of the five subjects at each speed. The upper and lower bounds are the maximal and minimal RMSEs, respectively, of the five subjects. The average RMSEs of ankle joint torques, knee joint torques, and hip joint torques at a walking speed of 0.8 m/s were 0.1920 Nm/kg, 0.1826 Nm/kg, and 0.1632 Nm/kg, respectively. The maximal RMSEs of the three joints at this walking speed were 0.2383 Nm/kg, 0.2372 Nm/kg, and 0.1850 Nm/kg, respectively. At a walking speed of 1.2 m/s, average RMSEs of 0.1822 Nm/kg, 0.2012 Nm/kg, and 0.1591 Nm/kg were obtained for the ankle, knee, and hip. The maximal RMSEs of the three joints at this walking speed were 0.2303 Nm/kg, 0.2670 Nm/kg, and 0.2338 Nm/kg. The average RMSEs of 0.2423 Nm/kg, 0.2375 Nm/kg, and 0.2289 Nm/kg and maximal RMSEs of 0.3481 Nm/kg, 0.3163 Nm/kg, and 0.2547 Nm/kg were calculated for the three joints when subjects walked at a speed of 1.6 m/s. Although the results of the interindividual testing were not as good as those of individual testing, most were acceptable, showing the relatively good generalizability of the proposed method. On the other hand, as the walking speed increased, the RMSEs of the results increased. This was because higher joint torques and a higher variable of joint torques were needed to adapt to the higher walking speed and control the lower extremities and balance of the torso.

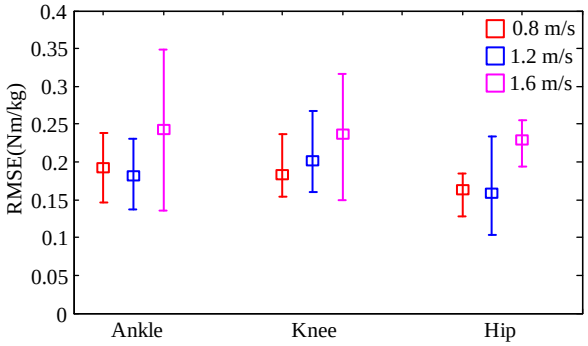

Fig. 14. RMS errors of interindividual testing.

VII. Discussion

The human gait is complex and is the result of fascinating cooperation between different joints and segments in the lower extremities [2]. For designing a high-level controller of exoskeletons, we expect that joint torque estimation can be achieved using as few as sensors to obtain reliable and comprehensive information. Foot motion and GRF are the direct indicators of human gait [12]. Fusing multisensor information on the human foot during walking is a convenient way to estimate joint torques. Soft smart shoes are developed in this study for motion intent learning at unspecified walking speeds, and LSTM with CAE is performed to explore deeper-layer structures and exploit the temporal connections between the measured signals. Therefore, the proposed strategy promises superior performance. The average time cost for estimating torques at a certain moment is about 2 ms when the predictor is developed using TensorFlow 2.0 and runs on a laptop (ThinkServer TS250, Lenovo, Ltd. Thus, it can meet the requirements of real-time control. However, at the same time, there are some limitations to this method. For example, the performance of the proposed learning strategy may decline at a speed that is very different from the trained speeds. In the future, gait information at various walking speeds should be incorporated in the training dataset to learn human motion intent at random and irregular walking speeds.

Generally speaking, ankle torques are the least variable, since the foot is constrained by the ground. On the contrary, the knee and hip are more variable, which is responsible for the control of the lower extremities and the balance of the torso [39]. Thus, estimating ankle torque has been investigated by many researchers [2]. However, the performance of the knee and hip remains unknown. In this study, about 98% of the total r^2 values of individual testing are acceptable. The performances of the learning algorithm may be a little better than the results in [2], in which a GP was adopted to estimate the ankle torques using the shank angles and angular velocities. Furthermore, how to obtain the shank angles and angular velocities outside of the lab was not addressed in [2]. RMSEs at a walking speed of 0.8 m/s were lower and fluctuated narrowly compared with the other two speeds. This is because higher joint torques and higher variables of joint torques are needed to adapt to the higher walking speed.

The results of interindividual testing are not as good as those of individual testing, which is expected, as gait patterns between subjects are not necessarily the same. In addition, the heights, masses, and leg lengths may vary considerably between subjects. If we expect a satisfactory result, the training dataset should be sufficient to build a universal model for unknown subjects. One goal of this study is to develop soft wearable shoes that have advantages, e.g., low cost, nonintrusive to the human gait, and comfortable to the wearers. The size of the smart shoe in this study is appropriate for the wearers to ensure comfort. In the future, several shoes of different sizes may be made when the shoe sizes of the wearers are different. The feasibility of motion intent learning using the novel soft smart shoe has been investigated. Thus, a knowledge base can be developed by measuring multisensor information of shoes of different sizes and age groups. Then, joint torques can be estimated as well as possible for designing a high-level controller.

Another issue that should be considered is that any information may contain noise. In some cases, the noisy information may deteriorate the learning results greatly. In this paper, a Kalman filter was adopted to remove the noise. IMUs fused with other sensors may be an alternative to improve the measurement accuracy. This point requires more investigation in the future. Moreover, it should be noted that a synchronization trigger should be used to keep the wearable sensing system and the reference system working simultaneously. In the study, the GRF was regarded as the trigger. When the GRF was measured by the force plate, the wearable sensing system began to measure the signals simultaneously.

VIII. Conclusions

A novel soft smart shoe was developed with a soft sole, two 3D motion sensors, and a self-designed data acquisition instrument to measure data on GRF and foot motion. The soft sole with a fiber-reinforced structure was made of silicone rubber. A “sensor image” was constructed for the measured signals which represented the spatial and temporal correlations among the multisensor data. It was feasible to use CNN to process signals, the same as for processing images. LSTM with CAE was developed to extract the hidden features of the sensor images and figure out the deep-layer relationships between joint torques and measurements. To the best of our knowledge, integrating LSTM and CAE for improving the performance of motion intent estimation has not yet been reported. The effectiveness and generalization of the proposed methodology were verified by individual testing and interindividual testing. In individual testing, 98% of the r^2 values were acceptable. The RSMEs implied a good agreement between the estimation and the reference. In interindividual testing, 75% of the r^2 values were acceptable. Although the results of interindividual testing were not as good as those of individual testing, most of the results were acceptable, showing the good generalizability of the proposed method. In summary, the feasibility of joint torque learning using the novel soft smart shoe and the proposed learning strategy has been verified.

In the future, a knowledge base can be developed by measuring multisensor information of feet. Then, the novel smart shoe developed in this study and the proposed learning algorithm can be put to practical use in applications like disease diagnosis, constructing a high-level controller for leg robots, etc.

References

[1] Zeng, Yan , et al., "Evolving Gaussian Process Autoregression Based Learning of Human Motion Intent Using Improved Energy Kernel Method of EMG." IEEE Transactions on Biomedical Engineering.2556-2565,2019.

[2] Eslamy, Mahdy, et al., "Synergy-based Gaussian Process Estimation of Ankle Angle and Torque: Conceptualization for High level Controlling of Active Robotic Foot Prostheses/Orthoses." Journal of Biomechanical Engineering-transactions of The Asme 141.2, 2019.

[3] Awad, Louis N., et al., "A soft robotic exosuit improves walking in patients after stroke."Science Translational Medicine 9.400, 2017.

[4] Thatte, Nitish, et al., "Robust and Adaptive Lower Limb Prosthesis Stance Control via Extended Kalman Filter-Based Gait Phase Estimation." international conference on robotics and automation, 3129-3136, 2019.

[5] Wang, Lukun. "Recognition of Human Activities Using Continuous Autoencoders with Wearable Sensors." Sensors 16.2: 189-189, 2016.

[6] Ye, Wenbin , et al., "Human Activity Classification Based on Micro-Doppler Signatures by Multiscale and Multitask Fourier Convolutional Neural Network." IEEE Sensors Journal 20.10(2020):5473-5479.

[7] Losey, et al., "A Review of Intent Detection, Arbitration, and Communication Aspects of Shared Control for Physical Human-Robot Interaction." Applied Mechanics Reviews 70.1: 010804-010804,2018.

[8] Zhang, Juanjuan, et al., "Human-in-the-loop optimization of exoskeleton assistance during walking." Science 356.6344: 1280-1284, 2017.

[9] Sartori, Massimo, et al., "Modeling and simulating the neuromuscular mechanisms regulating ankle and knee joint stiffness during human locomotion." Journal of Neurophysiology 114.4: 2509-2527,2015.

[10] Sartori, Massimo, et al., "EMG-Driven Forward-Dynamic Estimation of Muscle Force and Joint Moment about Multiple Degrees of Freedom in the Human Lower Extremity." PLOS ONE 7.12, 2012.

[11] Ao, Di, et al., "Movement Performance of Human–Robot Cooperation Control Based on EMG-Driven Hill-Type and Proportional Models for an Ankle Power-Assist Exoskeleton Robot." IEEE Transactions on Neural Systems and Rehabilitation Engineering 25.8: 1125-1134, 2017.

[12] Li, Guangyi, et al., "Wearable Sensor System for Detecting Gait Parameters of Abnormal Gaits: A Feasibility Study." IEEE Sensors Journal 18.10: 4234-4241, 2018.

[13] Ahmad, et al., "Human Action Recognition Using Deep Multilevel Multimodal (M2) Fusion of Depth and Inertial Sensors." IEEE Sensors Journal 20.3(2020):1445-1455.

[14] Li, Haobo , et al. "Bi-LSTM Network for Multimodal Continuous Human Activity Recognition and Fall Detection." IEEE Sensors Journal 20.3(2020):1191-1201.

[15] Chen, et al., "Multisensor Feature Fusion for Bearing Fault Diagnosis Using Sparse Autoencoder and Deep Belief Network." IEEE Transactions on Instrumentation and Measurement 66.7: 1693-1702, 2017.

[16] Ma, Xiaolei, et al., "Long short-term memory neural network for traffic speed prediction using remote microwave sensor data." Transportation Research Part C-emerging Technologies: 187-197, 2015.

[17] Edgar, S., et al., "Wearable shoe-based device for rehabilitation of stroke patients." international conference of the ieee engineering in medicine and biology society: 3772-3775, 2010.

[18] Ashutosh Tiwari, et al. "An Infrared Sensor-Based Instrumented Shoe for Gait Events Detection on Different Terrains and Transitions." IEEE Sensors Journal 20.18(2020):10779-10791.

[19] Zheng, Jianian , et al. "Designing Deep Reinforcement Learning Systems for Musculoskeletal Modeling and Locomotion Analysis Using Wearable Sensor Feedback." IEEE Sensors Journal 20.16(2020):9274-9282.

[20] He, Zexia, et al., "A Wearable Sensing and Training System: Towards Gait Rehabilitation for Elderly Patients With Knee Osteoarthritis." IEEE Sensors Journal 19.14: 5936-5945, 2019.

[21] Howell, et al., "Kinetic Gait Analysis Using a Low-Cost Insole."IEEE Transactions on Biomedical Engineering 60.12: 3284-3290, 2013.

[22] Kim, Jichul, , et al."Wearable sensor system including optical 3-axis GRF sensor for joint torque estimation in real-time gait analysis." international conference on advanced intelligent mechatronics: 112-117, 2014.

[23] Li, Guangyi, et al., "The Lower Limbs Kinematics Analysis by Wearable Sensor Shoes." IEEE Sensors Journal 16.8: 2627-2638, 2016.

[24] Choi, Hyunjin , et al., "A Soft Three-Axis Force Sensor Based on Radially Symmetric Pneumatic Chambers." IEEE Sensors Journal:1-1, 2019.

[25] Jentoft, Leif P., et al., "Flexible, stretchable tactile arrays from MEMS barometers."international conference on advanced robotics: 1-6, 2013.

[26] Hyo Seung Han, et al. "A Soft Ground Reaction Force Sensor System Utilizing Time-Delay Recurrent Neural Network." IEEE Sensors Journal 20.18(2020):10851-10861.

[27] Jacobs, et al., "Estimation of ground reaction forces and ankle moment with multiple, low-cost sensors." Journal of Neuroengineering and Rehabilitation 12.1: 90-90, 2015.

[28] Peng, Zhaoqin, et al., "Human falling recognition system design with wearable pressure sensing shoes." conference on industrial electronics and applications, 2017.

[29] Geng, Weidong, et al., "Gesture recognition by instantaneous surface EMG images.." Scientific Reports 6.1: 36571-36571, 2016.

[30] Yin, Y. , et al., "Dependant gaussian processes regression for intelligent sampling of freeform and structured surfaces" CIRP Annals - Manufacturing Technology, S000785061730063X.

[31] Sun, Wenjun, et al. "A sparse auto-encoder-based deep neural network approach for induction motor faults classification." Measurement: 171-178, 2016.

[32] Polygerinos, et al., "Soft robotic glove for combined assistance and at-home rehabilitation." Robotics and Autonomous Systems: 135-143, 2015.

[33] Potluri, Sasanka, et al. "Machine Learning based Human Gait Segmentation with Wearable Sensor Platform." international conference of the ieee engineering in medicine and biology society: 588-594, 2019.

[34] Razak, A., et al. "Foot Plantar Pressure Measurement System: A Review." Sensors 12.7: 9884-9912, 2012.

[35] Polygerinos, Panagiotis, et al., "Modeling of Soft Fiber-Reinforced Bending Actuators." IEEE Transactions on Robotics 31.3: 778-789, 2015.

[36] Fischer, et al., "Deep learning with long short-term memory networks for financial market predictions." European Journal of Operational Research 270.2: 654-669, 2017.

[37] Geng, Chi , et al., "Human Action Recognition based on Convolutional Neural Networks with a Convolutional Auto-Encoder." International Conference on Computer Sciences & Automation Engineering Atlantis Press, 2016..
[38] Qi, Shuhao , et al. "Recognition of Composite Motions based on sEMG via Deep Learning." 2019 14th IEEE Conference on Industrial Electronics and Applications (ICIEA) IEEE, 2019..
[39] Robertson, and D. Gordon E. Research methods in biomechanics.2013.
[40] Findlow, Andrew H., et al. "Predicting lower limb joint kinematics using wearable motion sensors.." Gait & Posture 28.1: 120-126, 2008.
[41] Bogey, Ross A. , et al., "An EMG-to-Force Processing Approach for Estimating in Vivo Hip Muscle Forces in Normal Human Walking." IEEE Transactions on Neural Systems and Rehabilitation Engineering 25.8: 1172-1179, 2017.

JianTao Yang was born in Hebei province, China. He received a BS degree in mechanical engineering from Yanshan University, Qinhuangdao, Hebei, China, in 2012, and an MA in mechatronics engineering from Yanshan University in 2015. He is currently working toward a PhD at the State Key Laboratory of Mechanical System and Vibration, Institute of Robotics, Shanghai Jiao Tong University, Shanghai, China. His research interests include control theory, robotic exoskeletons, and sensors.

YueHong Yin, State Key Laboratory of Mechanical System and Vibration, Institute of Robotics, Shanghai Jiao Tong University, Shanghai, China. He received a BE degree in mechanical engineering from the Nanjing Institute of Aeronautics, Nanjing, China, in 1990, and MS and PhD degrees from Nanjing University of Aeronautics and Astronautics, Nanjing, China, in 1995 and 1997, respectively. From December 1997 to December 1999, he was a Postdoctoral Fellow at Zhejiang University, Hangzhou, China, where he became an Associate Professor in July 1999. Since December 1999, he has been with the Robotics Institute, Shanghai Jiao Tong University, Shanghai, China, where he became a Professor in December 2005. His research interests include robotics, force control, and exoskeleton robots.